JCIM JOURNAL OF CHEMICAL INFORMATION AND MODELING

pubs.acs.org/jcim
Article

Quantitative Assessment of Energetic Contributions of Residues in a SARS-CoV-2 Viral Enzyme/Nanobody Interface

Amit Kumar and Harish Vashisth*

Cite This: J. Chem. Inf. Model. 2024, 64, 2068−2076
Read Online

ABSTRACT: The highly conserved protease enzyme from SARS-CoV-2 (M^{Pro}) is crucial for viral replication and is an attractive target for the design of novel inhibitory compounds. M^{Pro} is known to be conformationally flexible and has been stabilized in an extended conformation in a complex with a novel nanobody (NB2B4), which inhibits the dimerization of the enzyme via binding to an allosteric site. However, the energetic contributions of the nanobody residues stabilizing the M^{Pro}/nanobody interface remain unresolved. We probed these residues using all-atom MD simulations in combination with alchemical free energy calculations by studying the physical residue−residue interactions and discovered the role of hydrophobic and electrostatic interactions in stabilizing the complex. Specifically, we found via mutational analysis that three interfacial nanobody residues (Y59, R106, and L109) contributed significantly, two residues (L107 and P110) contributed moderately, and two residues (H112 and T113) contributed minimally to the overall binding affinity of the nanobody. We also discovered that the nanobody affinity could be enhanced via a charge-reversal mutation (D62R) that alters the local interfacial electrostatic environment of this residue in the complex. These findings are potentially useful in designing novel synthetic nanobodies as allosteric inhibitors of M^{Pro}.

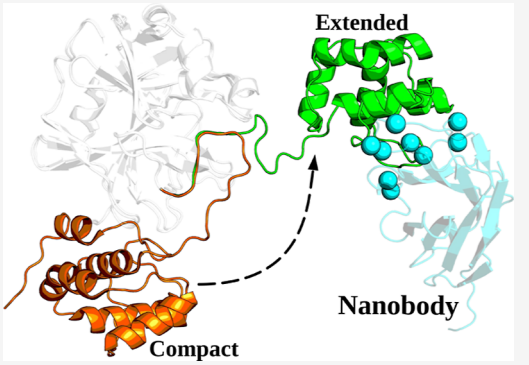

1. INTRODUCTION

Severe acute respiratory syndrome coronavirus 2 (SARS-CoV-2), the virus causing COVID-19, has presented a serious threat to human health.[1−4] Several effective vaccines mainly target the viral spike (S) protein, but the evolving variants of the virus (e.g., Delta[5] and Omicron[6]) have generated mutations in the S protein.[7−9] These mutations often reduce the efficacy of the vaccine, and as a result, alternate ways of targeting the virus continue to be explored. The highly conserved viral main protease (M^{Pro}; also known as 3C-like protease, $3CL^{Pro}$) plays an essential role in the viral replication process and is dissimilar to human protease enzyme.[10−13] Therefore, M^{Pro} is an attractive target for designing and developing novel, clinically effective agents against SARS-CoV-2.

The crystal structure of M^{Pro} revealed its conformation as a symmetric homodimer.[12,14−17] Each monomer in the homodimer comprises a catalytic domain (subclassified into domains I and II) and an α-helical domain (termed the domain III) which are connected by a long loop region (Figure 1). The dimeric form of M^{Pro} is known to be necessary for enzymatic activity.[18−20] Several studies have focused on blocking the formation of homodimer for designing new antiviral drugs.[13,21−25] The M^{Pro} dimer has also been targeted by both peptidomimetic and nonpeptidomimetic compounds.[12,26−32] Given that the proteases are dynamic and can take alternate conformations, there is strong experimental support for the notion that targeting intermediate conformations rather than the native state is an effective alternate strategy to regulate/

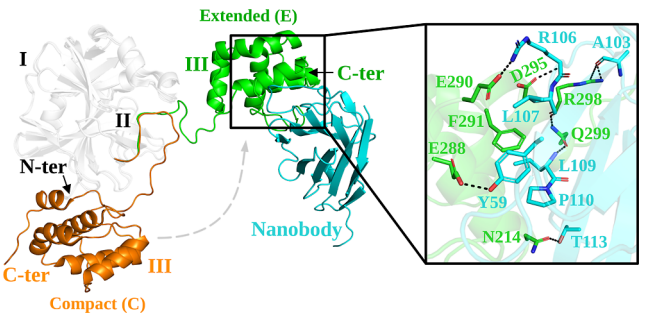

Figure 1. Structural details of the M^{Pro}/Nanobody protein−protein interaction. An overlay of the compact (labeled C) and extended/nanobody-bound (labeled E) conformations of M^{Pro}. The structural alignment is based on the domains labeled I and II (white). The α-helical domain (domain III) is shown in two states: the compact C state (orange) and the extended E state (green), along with the nanobody (cyan). A zoomed view of the residue−residue interactions in the M^{Pro}/nanobody interface is also shown. The M^{Pro} and nanobody residues are labeled in green and cyan, respectively.

Received: December 4, 2023
Revised: February 23, 2024
Accepted: February 26, 2024
Published: March 9, 2024

https://doi.org/10.1021/acs.jcim.3c01933
J. Chem. Inf. Model. 2024, 64, 2068−2076

block protein activity.[33] Recently, one such alternate conformation, an extended open conformation of M^{Pro} has been captured by a nanobody (NB2B4) molecule (cyan cartoon; Figure 1).[34] Biochemical and structural studies[34] suggest that the nanobody NB2B4 binds at an allosteric site in the α-helical domain, which is located away from the catalytic domain of M^{Pro} (Figure 1).

The crystal structure of the enzyme/nanobody complex suggests that the binding of the nanobody physically separates the N-terminal and the C-terminal domains of M^{Pro}, thereby inhibiting its dimerization and suppressing the enzymatic activity.[34] Furthermore, the crystal structure revealed that the aromatic moiety of F291, an M^{Pro} residue, inserts into a hydrophobic pocket composed of the nanobody residues Y59, L107, L109, and P110 (zoomed view; Figure 1). The mutation of F291 to A291 prevents the binding of the nanobody to M^{Pro}.[34] This study also revealed that the residue R106 in the nanobody molecule forms a salt-bridge with the side chains of the residues E290 and D295 of M^{Pro}.[34] The main chains of residues L107 and L109 from the nanobody form hydrogen bonds with the side chain of Q299 in M^{Pro}.[34] However, the precise energetic contributions of nanobody residues (involved in the interfacial interactions with the enzyme) toward the overall binding affinity between the nanobody and the protease enzyme are lacking. The knowledge of these energetic contributions is potentially useful for evolving new nanobodies against the protease.

In this study, we report all-atom MD simulations of wild-type (WT) and mutated nanobody complexes with M^{Pro} (Table S1 and Figure S1) and residue-specific free energy changes on mutations in those residues of the nanobody which physically contact the protease residues via a protein−protein interface (Figure 1a). The residue-specific free energy changes were quantified using the free energy perturbation (FEP)[35] method which was applied using an appropriate thermodynamic cycle (Figure S2).[36−39] Overall, we performed an aggregate of ∼24 μs of all-atom MD simulations and free energy calculations to provide the structural and energetic basis for the recognition of M^{Pro} by the nanobody. We also suggest mutations that can potentially enhance the affinity of the nanobody for M^{Pro}.

2. MATERIALS AND METHODS

2.1. Molecular Dynamics Setup. We conducted all-atom MD simulations of M^{Pro} in a complex with a nanobody (NB2B4). We derived the initial coordinates for the M^{Pro}/nanobody complex from the crystal structure (PDB code: 7VFB)[34] and modeled the missing residues using MODELLER.[40] We generated the atomic coordinates of M^{Pro} bound with several mutants of the nanobody (Y59G, D62R, R106A, R106K, L107G, L109G, P110G, H112A, and T113A) using VMD.[41] All systems were then solvated with explicit TIP3P water molecules in periodic simulation domains (Figure S1). For maintaining the ionic concentration (150 mM NaCl), we added ions to the bulk water. The structure of the M^{Pro}/nanobody complex was determined at a pH of 5.5.[34] The low pH could result in the protonation of charged residues (such as Asp and Glu). Therefore, we used the PropKa server for calculating the pK_a values of charged residues at the interface of the M^{Pro}/nanobody complex.[42] The proPka server predicted the pK_a values for Asp and Glu to be lower than 5.0, which are lower than the pH used for determining the structures. This suggests unprotonated states for Asp and Glu residues at the interface of the M^{Pro}/nanobody complex. Therefore, we considered unprotonated states of negatively charged residues (i.e., Asp and Glu) in our simulation setup. The final system sizes are given in Table S1, and the overall simulation setup is shown in Figure S1.

We used the conjugate gradient minimization algorithm to energy-minimize each system for a total of 2000 steps prior to running all-atom MD simulations. During the initial phase (30 ns) of MD equilibration, we restrained (k = 10 kcal/mol Å^2) all of the C_α atoms. We did not use any restraints during production MD simulations. We carried out all conventional MD simulations using the CHARMM36[43] force field with a 2 fs time-step in the *NPT* ensemble. We maintained the temperature and pressure at 310 K and 1 bar using the Langevin thermostat and Nosé−Hoover barostat, respectively. We used periodic boundary conditions in all simulations and computed the long-range electrostatic interactions using the Particle Mesh Ewald method,[44] coupled with tinfoil boundary conditions,[45−47] as used in other similar studies.[36] For systems with non-neutral states (nonzero net charge), a neutralizing uniform background charge is introduced to provide a correction to the electrostatic energy per periodic cell.[45,46] For the van der Waals interactions, we used a cutoff of 12 Å with smooth switching taking effect at 10 Å.

We subjected each model to a μs-long conventional MD simulation and saved configurations every 20 ps. We generated two trajectories for each model with an aggregate time of 20 μs. We used VMD software[41] for generating input files. We performed visualization, analysis, and postprocessing of simulation trajectories using VMD,[41] CPPTRAJ,[48] and PyMOL.[49] We performed conventional MD simulations and free energy calculations with NAMDv3.0,[45] which incorporates a new GPU implementation of the FEP method.

2.2. Alchemical Free Energy Calculations. Using the alchemical free energy simulation method,[35] we determined the energetic contribution of key amino acid residues in the nanobody for their binding to M^{Pro}. Specifically, we designed a thermodynamic cycle (Figure S2) where the vertical arms of the cycle correspond to binding of the nanobody to M^{Pro}, and the horizontal arms correspond to the alchemical transformation of a WT amino acid into a mutated amino acid in the nanobody. Since the physical binding of the nanobody (vertical arms in Figure S2) to M^{Pro} is not the focus of this study, we computed the free energy changes along the unphysical pathways in the complex (upper horizontal arm in Figure S2, ΔG^{comp}) and free nanobody in an aqueous environment (lower horizontal arm in Figure S2, ΔG^{free}) as $\Delta\Delta G = \Delta G^{comp} - \Delta G^{free} = \Delta G^{bind}$ (wild-type) $- \Delta G^{bind}$ (mutant).

We used a hybrid energy function (U_m) to represent a mixture of two end point states of a particular horizontal arm of the thermodynamic cycle (Figure S2). The molecular topology follows a dual topology strategy. A coupling parameter λ_m connects the initial (I) and the final (F) states by a series of equispaced intermediate states. The coupling parameter values λ_m = 0 and 1 correspond to the physical end states whereas an intermediate value corresponds to a mixed unphysical state. Using the previously described[36−38] FEP method, we obtained the total free energy changes along the horizontal paths by summing over the intermediate states in the following way: $\Delta G(I \rightarrow F) = G_F - G_I = -\beta^{-1} \sum_{m=1}^{n-1} \ln\langle \exp[-\beta(U_{m+1} - U_m)]\rangle_m$, where $U_m = (1 - \lambda_m)U_I +$

https://doi.org/10.1021/acs.jcim.3c01933
J. Chem. Inf. Model. 2024, 64, 2068−2076

$\lambda_m U_F$ with the coupling parameter λ_m varying from 0 to 1 and the total number of intermediate points $m = 1, ..., (n-1)$, β is $1/k_B T$, with k_B as Boltzmann's constant, and T is the temperature.

We set the value of "alchDecouple" to "OFF" in our free energy calculation protocol in order to scale the nonbonded interactions along the alchemical coordinate. This protocol allowed us to scale the nonbonded interactions of the mutated residue with their environment and within the mutated residue, which contribute to the cumulative free energy. Furthermore, in our free energy calculations, we decoupled the charges from $\lambda_m = 0$ to $\lambda_m = 0.5$ while the van der Waals parameters were decoupled from $\lambda_m = 0$ to $\lambda_m = 1$ using 25 equally spaced λ_m windows distributed over 30 ns simulations. We simulated each λ_m window for 1.2 ns and used the last 1 ns for estimating free energy. We averaged the total free energy change (ΔG^{free}, ΔG^{comp}) over forward and backward simulations and repeated them in triplicate with different initial velocities, yielding a minimum of 180 ns of simulation data per transformation (Tables S2−S4). We report free energy calculations with an aggregate time of ∼3.24 μs. We have reported the $\Delta\Delta G$ value as the difference in the averaged ΔG^{comp} and ΔG^{free} values.

We estimated the free energy differences using the bidirectional approach by incorporating samples from both forward and backward transformations. The related statistical error was calculated using the Bennet acceptance ratio estimator implemented in the ParseFEP toolkit[50] in VMD. To ensure the convergence, we compared the graphical representation of the underlying probability distributions characterizing the forward and backward transformations. We reported the uncertainty in the averaged ΔG^{comp} and ΔG^{free} as the standard error of the mean (from three replicas) and have calculated the error in the final $\Delta\Delta G$ by computing the standard error of the mean associated with the averaged ΔG values. We obtained a good convergence and a reasonable statistical uncertainty (<1 kcal/mol) of the computed energetics ($\Delta\Delta G$).[36,37,51]

3. RESULTS

3.1. Dynamics of the WT M^{Pro}/Nanobody Complex.

We first performed μs-scale all-atom MD simulations for the WT M^{Pro}/nanobody complex in explicit solvent (Table S1). To assess the structural flexibility of this complex, we monitored the root-mean-squared deviation (RMSD) relative to the initial structure. In Figure S3 (black traces labeled WT), we show the RMSD traces for the complex, domains I and II, domain III, and the nanobody. Briefly, these results show that the average RMSD of the complex is ∼7 Å (Figure S3a), primarily due to conformational flexibility in domains I and II (Figure S3b), that are connected via a loop with domain III (Figure 1), which also physically interacts with the nanobody. The RMSD traces of domain III (Figure S3c) and the nanobody (Figure S3d) reveal significant stability (RMSD < 3 Å). These trends are further consistent with the root-mean-squared fluctuation per residue (RMSF) computed for these domains and the nanobody (Figure S4, see also Supporting Information Results).

To investigate the impact of noncovalent interactions on the affinity of the nanobody for M^{Pro}, we performed an interaction energy decomposition analysis for each interfacial residue of the nanobody with all residues in M^{Pro}. This allowed us to explore the specific contribution of noncovalent interactions in shaping the nanobody's affinity for M^{Pro}. The interaction energy is the sum of the electrostatic energy and the van der Waals energy. For each MD trajectory, we used the NAMD energy plugin in VMD[41] to calculate the interaction energies. In these energy calculations, we used the force field parameters from MD simulations, the nonbonded cutoff used in conducting MD simulations, as well as the Particle Mesh Ewald method[44] for computing electrostatic interactions. It should be noted that the nonbonded energy of a given interfacial residue of the nanobody is not its absolute binding affinity but is an approximate indicator of the binding affinity emerging from noncovalent interactions of a particular residue with the atoms in M^{Pro}.

We observed that several residues of the nanobody (Y59, A103, R106, L107, L109, P110, H112, and T113) revealed favorable interactions as characterized by the negative interaction energies with M^{Pro} (Figure 2a). Specifically, residue R106 of the nanobody showed the strongest interaction energy (−72.18 ± 3.16 kcal/mol) followed by residue Y59 (−30.93 ± 1.10 kcal/mol). The residues A103, L107, L109, P110, H112, and T113 showed interaction energies ranging between ∼−7 and ∼−14 kcal/mol. The side chains of residues L107, L109,

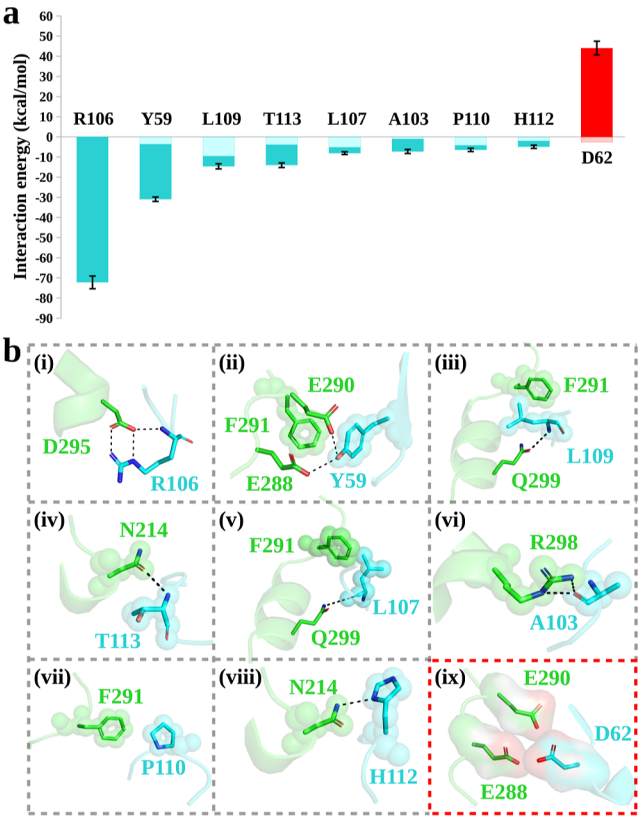

Figure 2. Nonbonded interaction energy analysis and structural insights from MD simulations of the WT M^{Pro}/nanobody complex. The nonbonded interaction energies (panel a) and a zoomed view of key residue level interactions (panel b) is shown. The interaction energy was computed between each nanobody residue at the interface and all residues of M^{Pro}. The bars are color-coded to represent different interaction energies. The dark color indicates the electrostatic interaction energy, while the light color corresponds to the van der Waals interaction energy. The residue level interactions (black dotted lines, polar interactions) are based on the dominant cluster obtained by clustering MD trajectories using CPPTRAJ.[48] Selected amino acids are represented as sticks, spheres, and surfaces. The fractional occupancies of these interactions are shown in Figure S8a.

https://doi.org/10.1021/acs.jcim.3c01933
J. Chem. Inf. Model. 2024, 64, 2068−2076

and P110 along with the side chain of residue Y59 were suggested to form a hydrophobic pocket. The interaction energies of these residues (L107, L109, and P110) with M^{Pro} are −8.07 ± 0.68, −14.62 ± 1.27, and −6.45 ± 0.80 kcal/mol, respectively. The van der Waals interaction energy contribution by residues involved in the formation of a hydrophobic pocket (Y59, L107, L109, and P110) ranges between ∼−4 and ∼−9 kcal/mol. While eight interfacial residues of the nanobody showed favorable interactions with M^{Pro}, residue D62 showed an unfavorable interaction energy (41.50 ± 3.40 kcal/mol; red bar in Figure 2a). We now describe specific residue level interactions underlying these favorable/unfavorable interaction energy trends.

The specific residue level interactions at the M^{Pro}/nanobody interface computed based on MD simulations of the WT complex are shown in Figures 2b and S5a. These data show that residue R106 (nanobody) interacts with D295 (M^{Pro}) via salt bridges and hydrogen bonds formed by the following interatomic interactions: R106@NH1···D295@OD1, R106@NE···D295@OD2, and R106@N···D295@OD2 with occupancies of 93, 90, and 53%, respectively (Figure S8a). The residue Y59 (nanobody) forms hydrogen bonding interactions with E288 and E290 (M^{Pro}), involving the interatomic interactions Y59@OH···E288@OE2 and Y59@OH···E290@OE2, with occupancies of 78 and 40%, respectively (Figure S8a). The side chain of residue Y59 also forms hydrophobic interactions with F291 (M^{Pro}) (Figure 2b).

The side chains of residues L107, L109, and P110 (nanobody) form hydrophobic interactions with F291 (M^{Pro}) (Figure 2b), and the side chain of H112 (nanobody) forms a hydrogen bond with residue N214 (M^{Pro}), which has an occupancy of 60% (Figure S8a). The side chain of residue T113 stacks over the side chain of residue N214 (M^{Pro}) and the backbone of T113 forms an interatomic interaction [Figure 2b, panel (iv)] as T113@N···N214@OD1 with a 95% occupancy (Figure S8a). The side chain of residue A103 (nanobody) is not involved in any interaction, although non-side-chain atoms are located near residue R298 (M^{Pro}). Moreover, the positive interaction energy (unfavorable interactions) for residue D62 is due to its side chain being oriented toward the negatively charged residues E288 and E290 (M^{Pro}) resulting in repulsive interactions. These observations from conventional MD simulations suggest that a network of hydrophobic and electrostatic interactions, primarily originating in the nanobody residues (Y59, A103, R106, L107, L109, P110, H112, and T113), are involved in the recognition of M^{Pro} by the nanobody.

3.2. Mutations in the Interfacial Residues of the Nanobody Alter Its Binding Affinity to M^{Pro}. To quantify the effect of mutations in the nanobody on its binding affinity to M^{Pro}, we have utilized a computationally rigorous FEP methodology[35−38] for computing the binding affinity of WT and mutated forms of the nanobody toward M^{Pro}. Our conventional all-atom MD simulations of the WT M^{Pro} bound to the nanobody suggest that a network of electrostatic and hydrophobic interactions is involved in the recognition of M^{Pro}. These simulations also suggest that eight interfacial residues of the nanobody (Y59, A103, R106, L107, L109, P110, H112, and T113) have stronger interaction energies with M^{Pro} and contribute significantly toward the overall binding energy of the nanobody. Therefore, we mutated each of these residues individually to glycine or alanine, except residue A103, which had no side-chain interactions with residues in M^{Pro}.

Specifically, we mutated residues involved in hydrophobic interactions (Y59, L107, L109, and P110) to glycine residues and those involved in electrostatic interactions (R106, H112, and T113) to alanine residues. Mutating protein residues involved in hydrophobic interactions into glycines is a commonly employed strategy in protein engineering and structural biology[38,52−54] because glycine is the smallest residue, completely devoid of a side chain and is highly flexible,[54] therefore, it can disrupt hydrophobic packing. Similarly, mutating residues involved in electrostatic interactions into alanines is a well-established approach for investigating the role of electrostatic interactions because alanine is relatively inert and has minimal steric impact.[55−58]

Moreover, given the repulsive interactions of residue D62, as observed in conventional MD simulations [Figure 2b, panel (ix)], we hypothesized that mutating this residue to a positively charged residue (R62) may alter the local electrostatic environment toward favorable interactions and possibly enhance the binding affinity of the nanobody. Additionally, given the salt-bridging interactions of the nanobody residue R106 with D295 of M^{Pro} and the strongest interaction energy observed in MD simulations [Figure 2b, panel (i)], we tested whether mutating R106 to K106, a conservative mutation to an amino acid (lysine) having a shorter side chain, will affect the overall binding affinity of the nanobody for M^{Pro}. The computed relative free energy changes ($\Delta\Delta G$) resulting from these mutations are listed in Tables S2−S4, shown in Figures 3−5, and described below.

3.3. Energetics of Glycine Mutations: Y59G, L107G, L109G, and P110G. In Figure 3a, we show the calculated relative changes in the binding free energy upon glycine mutations in four nanobody residues (Y59G, L107G, L109G, and P110G). Two of these mutations impose high energetic penalties and reduce the binding affinity of the nanobody by more than 6 kcal/mol: L109G ($\Delta\Delta G$ = 7.13 ± 0.23 kcal/mol) and Y59G ($\Delta\Delta G$ = 6.05 ± 0.30 kcal/mol). The other two mutations moderately reduce the binding affinity of the nanobody by ∼3−4 kcal/mol: L107G ($\Delta\Delta G$ = 3.60 ± 0.35 kcal/mol) and P110G ($\Delta\Delta G$ = 3.04 ± 0.44 kcal/mol).

To probe changes in residue level interactions due to glycine mutations, we analyzed the structures representing the dominant conformational cluster derived from an ensemble of conformations sampled via MD simulations of the mutated M^{Pro}/nanobody complexes. For all glycine mutations (Y59G, L107G, L109G, and P110G), we show representative snapshots of interaction patterns before and after the mutation in the M^{Pro}/nanobody protein−protein interface (Figures 3b, S5b−d, and S6a). We observed that the L109G mutation resulted in disruption of hydrophobic interactions with M^{Pro} residue F291 while a new salt bridge is established between residues R106 (M^{Pro}) and E290 (nanobody) (Figures 3b and S5b). The backbone interaction with M^{Pro} residue Q299 (G109@N···Q299@OE1) remains intact (Figures 3b and S8b). For the Y59G mutation, the interactions with M^{Pro} residues E288 and F291 are disrupted (Figure 3b). This mutation also induced the formation of a new hydrogen bond between nanobody residue H112 and M^{Pro} residue N214 (H112@N···N214@OD1) which showed an occupancy of 95% (Figures S5c and S8c). The L107G mutation resulted in disruption of hydrophobic interactions with M^{Pro} residue F291 while keeping the backbone interaction intact with M^{Pro} residue Q299 (G107@O···Q299@NE2) (Figures 3b, S5d, and S8d). Furthermore, we observed that the P110G mutation

https://doi.org/10.1021/acs.jcim.3c01933
J. Chem. Inf. Model. 2024, 64, 2068−2076

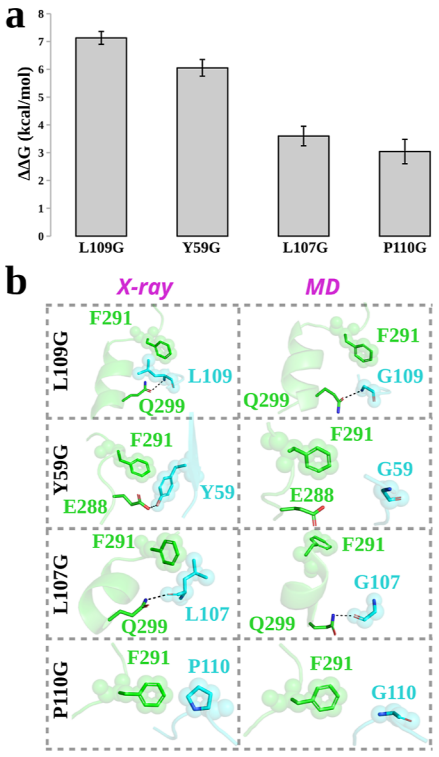

Figure 3. Energetics of glycine mutations in the nanobody and associated structural changes in the M^{Pro}/nanobody interface. Shown are the relative binding free energy ($\Delta\Delta G$) values (panel a) for glycine mutations in key nanobody residues involved in the protein−protein interface with M^{Pro}. For each mutation, an initial (X-ray) snapshot and a final (after mutation) snapshot are shown (panel b) where amino acids from M^{Pro} and nanobody are uniquely colored and labeled. On mutations, the fractional occupancies of key interactions (black dotted lines) for residues in the interface are shown in Figures S8b−d and S9a.

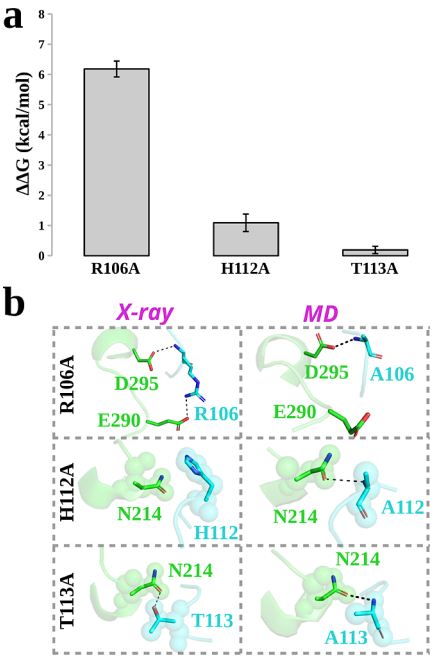

Figure 4. Data similar to Figure 3 are shown for three alanine mutations (R106A, H112A, and T113A) in the nanobody: (a) relative free energy values and (b) structural comparison. See also Figures S6b−d and S9b−d.

resulted in the disruption of hydrophobic interactions with M^{Pro} residue F291 (Figures 3b, S6a, and S9a).

3.4. Energetics of Alanine Mutations: R106A, H112A, and T113A. In Figure 4a, we show the calculated relative changes in the binding free energies upon alanine mutations in three nanobody residues (R106A, H112A, and T113A). These calculations reveal that mutation R106A imposes a high energetic penalty ($\Delta\Delta G$ = 6.18 ± 0.26 kcal/mol) and reduces the binding affinity of the nanobody by more than 6 kcal/mol. The remaining two mutations only marginally reduce the nanobody affinity by ∼0.19−1.09 kcal/mol relative to the WT nanobody: H112A ($\Delta\Delta G$ = 1.09 ± 0.29 kcal/mol) and T113A ($\Delta\Delta G$ = 0.19 ± 0.12 kcal/mol).

Furthermore, we probed the structural changes in residue level interactions due to alanine mutations (R106A, H112A, and T113A). In Figure 3b, we show that the R106A mutation disrupted the side-chain interactions with M^{Pro} residue E290 while the backbone interaction with D295 remains intact (Figure 4b). This mutation also led to the formation of new interaction between nanobody residue G104 and M^{Pro} residue R298 (G104@N···R298@NH1) and between nanobody residue H112 and M^{Pro} residue N214(H112@N···N214@OD1), which showed occupancies of 68 and 92%, respectively (Figures S6b and S9b). Other two mutations H112A and T113A in the nanobody induced the formation of new hydrogen bonds between the mutated nanobody residues and M^{Pro} residue N214 (as A112@N···N214@OD1; A113@N···N214@OD1, respectively) (Figures 4b, S6c,d, and S9c,d).

3.5. Energetics of Novel Mutations: R106K and D62R. We further tested two novel mutations (R106K and D62R) in the nanobody, where R106K is a conservative mutation to a shorter side chain of lysine and D62R is a charge-reversal mutation to alter the local electrostatic environment. Our $\Delta\Delta G$ calculations showed that conservative mutation R106K marginally reduced the binding affinity ($\Delta\Delta G$ = 3.38 ± 0.15 kcal/mol) of the nanobody, thereby highlighting the importance of the R106 residue in favorably stabilizing the nanobody in the WT complex. The structural origin of this reduction in the binding affinity of the nanobody can be attributed to a loss in salt-bridging interactions because the side chain of K106 forms only one salt-bridging interaction with D295 (M^{Pro}) as K106@NZ···D295@OD2 with an occupancy of 62%, as opposed to two salt-bridging interactions observed for R106 (Figures 5a, S7a, and S10a). In contrast, charge-reversal mutation D62R indeed strengthened the binding affinity ($\Delta\Delta G$ = −4.77 ± 0.54 kcal/mol) of the nanobody, consistent with the hypothesis that altering the locally repulsive electrostatic environment of this residue may improve the binding affinity of the nanobody. This is due to the formation of a new salt-bridging interaction network, involving R62 (nanobody) and M^{Pro} residue E288 (as R62@NH1···E288@OE2, R62@NE···E288@OE1), as well as involving G104 (nanobody) and R298 (M^{Pro}) as G104@O···R298@NH2 (Figures 5b and S7b). These interactions showed >70% occupancies (Figure S10b).

4. DISCUSSION

The highly conserved protease enzyme (M^{Pro}) is an attractive target for designing effective anti-SARS-CoV-2 agents. Recently, a nanobody molecule has been observed to capture M^{Pro} in an extended open conformation by binding to an

https://doi.org/10.1021/acs.jcim.3c01933
J. Chem. Inf. Model. 2024, 64, 2068−2076

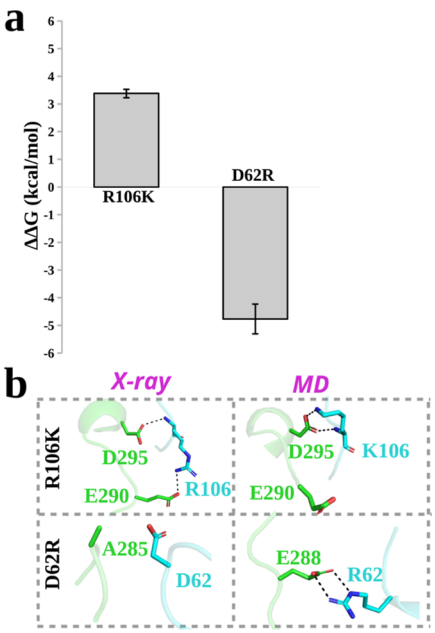

Figure 5. Data similar to Figure 3 are shown for two novel mutations (R106K and D62R) in the nanobody: (a) relative free energy values, and (b) structural comparison. See also Figures S7 and S10.

allosteric site located away from its catalytic subdomain (Figure 1).[34] Although the crystal structure of the M^{Pro}/nanobody complex has provided molecular insights into viral M^{Pro} recognition by the nanobody, the precise energetic contributions of nanobody residues involved in interfacial interactions with the enzyme, influencing the overall binding affinity between the nanobody and protease enzyme, remain unknown. Understanding these energetic contributions is crucial for developing new nanobodies targeting M^{Pro}. Therefore, we address these questions using all-atom MD simulations combined with the alchemical free energy calculations. Specifically, we investigated dynamics of the WT and mutant M^{Pro}/nanobody complexes, the nonbonded interactions between the interfacial nanobody residues and M^{Pro}, and the free energy changes on mutations in the nanobody. Furthermore, we propose potential mutations that can enhance the affinity of the nanobody toward M^{Pro}.

We first performed calculations to determine the nonbonded interaction energy between the interfacial nanobody residues and all residues within M^{Pro}. This analysis aimed to explore the extent to which the interfacial nanobody residues contributed to the overall binding affinity of the nanobody toward M^{Pro}. The magnitudes of nonbonded interaction energies suggested that several nanobody residues (Y59, A103, R106, L107, L109, P110, H112, and T113) showed stronger interaction energies and likely played a significant role in binding to M^{Pro}. Particularly, residue R106 of the nanobody showed the strongest interaction energy (∼−72 kcal/mol), followed by residue Y59 (∼−30 kcal/mol). The remaining residues (A103, L107, L109, P110, H112, and T113) showed favorable interaction energies ranging between ∼−7 and ∼−14 kcal/mol (Figure 2a). However, we observed an unfavorable interaction energy (∼+41 kcal/mol) for residue D62. Overall, the structural and energetic analysis of residue level interactions at the M^{Pro}/nanobody interface revealed a network of hydrophobic and electrostatic interactions, predominantly originating from specific nanobody residues (Y59, A103, R106, L107, L109, P110, H112, and T113) (Figure 2b). These findings shed light on the specific residues within the nanobody that contribute significantly to binding to M^{Pro}.

Based on the residue level interaction energy analysis for the M^{Pro}/nanobody interface, we further conducted rigorous free energy calculations to investigate the impact of mutations on key nanobody residues (Y59, D62, R106, L107, L109, P110, H112, and T113). Our free energy data revealed that relative to the WT M^{Pro}/nanobody complex, the mutations in three nanobody residues (Y59G, R106A, and L109G) were most detrimental, resulting in a decrease in the nanobody binding affinity by over 6 kcal/mol (Figures 3a and 4a). Two mutations (L107G and P110G) had a moderately detrimental effect, decreasing the nanobody affinity by ∼3−4 kcal/mol, while the mutations H112A and T113A had the least detrimental effect, decreasing the nanobody affinity by ∼0.19−1.09 kcal/mol. Overall, both glycine and alanine mutations negatively impacted the nanobody binding affinity ($\Delta\Delta G$ ranging between ∼0.19 and ∼7.13 kcal/mol), thereby reaffirming the importance of hydrophobic and electrostatic interactions in stabilizing the binding of the nanobody to M^{Pro}. Additionally, we assessed two novel mutations (D62R and R106K) that might alter the nanobody binding affinity. Our data showed that the charge-reversal mutation (D62R) is indeed favorable because it alters the locally repulsive electrostatic environment of D62 and enhances the nanobody binding affinity by ∼−5 kcal/mol while the R106K mutation, though a conservative substitution, is unfavorable due to the loss of some salt-bridging interactions, thereby decreasing the binding affinity of the nanobody by ∼3 kcal/mol (Figure 5a).

Moreover, we investigated alterations in residue level interactions caused by mutations in the M^{Pro}/nanobody complexes. Notably, the Y59G mutation disrupted interactions with M^{Pro} residues E288 and F291 (Figure 3b). For the L109G mutation, interactions with M^{Pro} residue F291 are disrupted (Figure 3b). Similarly, the R106A mutation disrupted interactions with M^{Pro} residue E290 (Figure 4b). On the other hand, the affinity-enhancing mutation (D62R) resulted in the formation of a salt-bridge interaction network (Figure 5b), involving R62 (nanobody) and M^{Pro} residue E288, as well as induced the formation of an interaction between residue G104 (nanobody) and R298 (M^{Pro}) (Figure S7b). Furthermore, we observed that the R106 K mutation showed less favorability (Figure 5a) as K106 formed only one salt-bridging interaction with D295 (M^{Pro}) with an occupancy of 62% (Figure 5b), in contrast to two such interactions between R106 and D295, with an occupancy greater than 90% (Figures S7a and S10a). Consequently, the longer side chain of R106 is crucial for optimal salt-bridging interactions with D295 (M^{Pro}). The mutation of R106 to K106 disrupts these interactions and results in a reduced overall binding affinity for the nanobody. Briefly, we also note that the relative binding free energies ($\Delta\Delta G$) are reported in our work, and any effects due to change in the net charge of the system due to a mutation are expected to cancel out during the thermodynamic cycle. Moreover, all simulations were conducted using the Particle Mesh Ewald method[44] with tinfoil boundary conditions,[45−47] and a neutralizing uniform background charge in non-neutral states to provide a correction to the electrostatic energy per periodic cell.[45,46] However, systematic studies of finite-size effects in free energy calculations, as have been studied for some specific cases,[59,60] may be needed to further improve future protocols. Overall, these calculations further enhance

https://doi.org/10.1021/acs.jcim.3c01933
J. Chem. Inf. Model. 2024, 64, 2068−2076

our understanding of the experimental structural data on this complex by providing a quantitative assessment of the significance of interfacial residues involved in the recognition of M^{Pro} by the nanobody. Moreover, these results provide guidance for the future design of novel nanobodies targeting the SARS-CoV-2 protease enzyme.

5. CONCLUSION

We have investigated the dynamic behavior of the SARS-CoV-2 main protease (M^{Pro}) when complexed with a nanobody in an extended conformation. We further examined the impact of nanobody mutations on the binding interaction. Our findings suggest that the nanobody utilizes a combination of hydrophobic and electrostatic interactions to effectively bind with M^{Pro}. Notably, the D62R mutation in the nanobody enhances the overall binding affinity for M^{Pro}. The molecular insights gained from our quantitative assessment of the nanobody residues are potentially valuable in the future development of synthetic nanobodies with improved binding affinity, potentially serving as potent allosteric inhibitors of M^{Pro} dimerization in SARS-CoV-2.

■ ASSOCIATED CONTENT

Data Availability Statement

All methodological details for all data generated in this study are available in the Materials and Methods section including PDB codes of input files, simulation conditions, and error analysis. The input files for conventional MD simulations and FEP calculations for mutations in the M^{Pro}/nanobody complex are available at github: (https://github.com/amit9869/MPro-Nanobody.git). The free energy data averaged over forward and backward transformations for each mutation in complex and solution are also provided (Tables S2−S4). The simulation and visualization softwares[41,45,49,61] and the force field[43] used to carry out calculations are openly available.

Supporting Information

The Supporting Information is available free of charge at https://pubs.acs.org/doi/10.1021/acs.jcim.3c01933.

> Additional data and analyses, steps for system setup and MD simulations, thermodynamic cycle for estimating the relative binding free energy of mutations in the nanobody, RMSD and root-mean-squared fluctuation (RMSF) of the M^{Pro}/nanobody complexes, fractional occupancies of all key interactions, and structural insights from MD simulations of the M^{Pro}/nanobody complexes (PDF)

■ AUTHOR INFORMATION

Corresponding Author

Harish Vashisth − *Department of Chemical Engineering and Bioengineering, University of New Hampshire, Durham, New Hampshire 03824, United States;* orcid.org/0000-0002-2087-2880; Phone: +1-603-862-2483; Email: harish.vashisth@unh.edu

Author

Amit Kumar − *Department of Physics and Astronomy, Wayne State University, Detroit, Michigan 48201, United States*

Complete contact information is available at: https://pubs.acs.org/10.1021/acs.jcim.3c01933

Notes

The authors declare no competing financial interest.

■ ACKNOWLEDGMENTS

We acknowledge the financial support provided by the National Institutes of Health (NIH) through grant R35GM138217. We are grateful for computational support through the following resources: Premise, a central shared HPC cluster at UNH supported by the Research Computing Center and BioMade, a heterogeneous CPU/GPU cluster supported by the NSF EPSCoR award (OIA-1757371).

■ REFERENCES

(1) Hasöksüz, M.; Kilic, S.; Sarac, F. Coronaviruses and SARS-CoV-2. *Turk. J. Med. Sci.* **2020**, *50*, 549−556.

(2) Zhu, N.; Zhang, D.; Wang, W.; Li, X.; Yang, B.; Song, J.; Zhao, X.; Huang, B.; Shi, W.; Lu, R.; Niu, P.; Zhan, F.; Ma, X.; Wang, D.; et al. A novel coronavirus from patients with pneumonia in China, 2019. *N. Engl. J. Med.* **2020**, *382*, 727−733.

(3) Zheng, J. SARS-CoV-2: an emerging coronavirus that causes a global threat. *Int. J. Biol. Sci.* **2020**, *16*, 1678−1685.

(4) Delahay, R. J.; de la Fuente, J.; Smith, G. C.; Sharun, K.; Snary, E. L.; Flores Giron, L.; Nziza, J.; Fooks, A. R.; Brookes, S. M.; Lean, F. Z.; Breed, A. C.; et al. Assessing the risks of SARS-CoV-2 in wildlife. *One Health Outlook* **2021**, *3*, 7.

(5) Mlcochova, P.; Kemp, S. A.; Dhar, M. S.; Papa, G.; Meng, B.; Ferreira, I. A.; Datir, R.; Collier, D. A.; Albecka, A.; Singh, S.; Pandey, R.; Brown, J.; Zhou, J.; Goonawardane, N.; et al. SARS-CoV-2 B.1.617. 2 Delta variant replication and immune evasion. *Nature* **2021**, *599*, 114−119.

(6) Fan, Y.; Li, X.; Zhang, L.; Wan, S.; Zhang, L.; Zhou, F. SARS-CoV-2 Omicron variant: recent progress and future perspectives. *Signal Transduction Targeted Ther.* **2022**, *7*, 141.

(7) Salvatori, G.; Luberto, L.; Maffei, M.; Aurisicchio, L.; Roscilli, G.; Palombo, F.; Marra, E. SARS-CoV-2 SPIKE PROTEIN: an optimal immunological target for vaccines. *J. Transl. Med.* **2020**, *18*, 222.

(8) Martinez-Flores, D.; Zepeda-Cervantes, J.; Cruz-Resendiz, A.; Aguirre-Sampieri, S.; Sampieri, A.; Vaca, L. SARS-CoV-2 vaccines based on the spike glycoprotein and implications of new viral variants. *Front. Immunol.* **2021**, *12*, 701501.

(9) Souza, P. F. N.; Mesquita, F. P.; Amaral, J. L.; Landim, P. G.; Lima, K. R.; Costa, M. B.; Farias, I. R.; Belém, M. O.; Pinto, Y. O.; Moreira, H. H.; Magalhaes, C.; Castelo-Branco, D.; Montenegro, R.; Andrade, C. R. The spike glycoproteins of SARS-CoV-2: A review of how mutations of spike glycoproteins have driven the emergence of variants with high transmissibility and immune escape. *Int. J. Biol. Macromol.* **2022**, *208*, 105.

(10) Thiel, V.; Ivanov, K. A.; Putics, A.; Hertzig, T.; Schelle, B.; Bayer, S.; Weißbrich, B.; Snijder, E. J.; Rabenau, H.; Doerr, H. W.; Gorbalenya, A. E.; Ziebuhr, J. Mechanisms and enzymes involved in SARS coronavirus genome expression. *J. Gen. Virol.* **2003**, *84*, 2305−2315.

(11) Ziebuhr, J. Molecular biology of severe acute respiratory syndrome coronavirus. *Curr. Opin. Microbiol.* **2004**, *7*, 412−419.

(12) Mengist, H. M.; Dilnessa, T.; Jin, T. Structural basis of potential inhibitors targeting SARS-CoV-2 main protease. *Front. Chem.* **2021**, *9*, 622898.

(13) Ullrich, S.; Nitsche, C. The SARS-CoV-2 main protease as drug target. *Bioorg. Med. Chem. Lett.* **2020**, *30*, 127377.

(14) Dai, W.; Zhang, B.; Jiang, X.-M.; Su, H.; Li, J.; Zhao, Y.; Xie, X.; Jin, Z.; Peng, J.; Liu, F.; Li, C.; Li, Y.; Bai, F.; et al. Structure-based design of antiviral drug candidates targeting the SARS-CoV-2 main protease. *Science* **2020**, *368*, 1331−1335.

(15) Douangamath, A.; Fearon, D.; Gehrtz, P.; Krojer, T.; Lukacik, P.; Owen, C. D.; Resnick, E.; Strain-Damerell, C.; Aimon, A.; Ábrányi-Balogh, P.; Brandão-Neto, J.; Carbery, A.; Davison, G.; Dias,

A.; et al. Crystallographic and electrophilic fragment screening of the SARS-CoV-2 main protease. *Nat. Commun.* **2020**, *11*, 5047.
(16) Gao, K.; Wang, R.; Chen, J.; Tepe, J. J.; Huang, F.; Wei, G.-W. Perspectives on SARS-CoV-2 main protease inhibitors. *J. Med. Chem.* **2021**, *64*, 16922−16955.
(17) Zhao, Y.; Zhu, Y.; Liu, X.; Jin, Z.; Duan, Y.; Zhang, Q.; Wu, C.; Feng, L.; Du, X.; Zhao, J.; Shao, M.; Zhang, B.; Yang, X.; Wu, L.; Ji, X.; et al. Structural basis for replicase polyprotein cleavage and substrate specificity of main protease from SARS-CoV-2. *Proc. Natl. Acad. Sci. U.S.A.* **2022**, *119*, No. e2117142119.
(18) Anand, K.; Palm, G. J.; Mesters, J. R.; Siddell, S. G.; Ziebuhr, J.; Hilgenfeld, R. Structure of coronavirus main proteinase reveals combination of a chymotrypsin fold with an extra alpha-helical domain. *EMBO J.* **2002**, *21*, 3213−3224.
(19) Anand, K.; Ziebuhr, J.; Wadhwani, P.; Mesters, J. R.; Hilgenfeld, R. Coronavirus main proteinase ($3CL^{pro}$) structure: basis for design of anti-SARS drugs. *Science* **2003**, *300*, 1763−1767.
(20) Noske, G. D.; Nakamura, A. M.; Gawriljuk, V. O.; Fernandes, R. S.; Lima, G. M.; Rosa, H. V. D.; Pereira, H. D.; Zeri, A. C.; Nascimento, A. F.; Freire, M. C.; Fearon, D.; et al. A crystallographic snapshot of SARS-CoV-2 main protease maturation process. *J. Mol. Biol.* **2021**, *433*, 167118.
(21) Vandyck, K.; Deval, J. Considerations for the discovery and development of 3-chymotrypsin-like cysteine protease inhibitors targeting SARS-CoV-2 infection. *Curr. Opin. Virol.* **2021**, *49*, 36−40.
(22) Unoh, Y.; Uehara, S.; Nakahara, K.; Nobori, H.; Yamatsu, Y.; Yamamoto, S.; Maruyama, Y.; Taoda, Y.; Kasamatsu, K.; Suto, T.; Kouki, K.; Nakahashi, A.; Kawashima, S.; Sanaki, T.; et al. Discovery of S-217622, a noncovalent oral SARS-CoV-2 3CL protease inhibitor clinical candidate for treating COVID-19. *J. Med. Chem.* **2022**, *65*, 6499−6512.
(23) Kneller, D. W.; Li, H.; Phillips, G.; Weiss, K. L.; Zhang, Q.; Arnould, M. A.; Jonsson, C. B.; Surendranathan, S.; Parvathareddy, J.; Blakeley, M. P.; Coates, L.; Louis, J. M.; Bonnesen, P. V.; et al. Covalent narlaprevir-and boceprevir-derived hybrid inhibitors of SARS-CoV-2 main protease. *Nat. Commun.* **2022**, *13*, 2268.
(24) Abdelnabi, R.; Foo, C. S.; Jochmans, D.; Vangeel, L.; De Jonghe, S.; Augustijns, P.; Mols, R.; Weynand, B.; Wattanakul, T.; Hoglund, R. M.; Tarning, J.; Mowbray, C. E.; Sjö, P.; et al. The oral protease inhibitor (PF-07321332) protects Syrian hamsters against infection with SARS-CoV-2 variants of concern. *Nat. Commun.* **2022**, *13*, 719.
(25) Jochmans, D.; Liu, C.; Donckers, K.; Stoycheva, A.; Boland, S.; Stevens, S. K.; De Vita, C.; Vanmechelen, B.; Maes, P.; Trüeb, B.; Ebert, N.; Thiel, V.; De Jonghe, S.; Vangeel, L.; Bardiot, D.; et al. The substitutions L50F, E166A, and L167F in SARS-CoV-2 3CLpro are selected by a protease inhibitor in vitro and confer resistance to nirmatrelvir. *mBio* **2023**, *14*, No. e02815.
(26) Zhang, L.; Lin, D.; Sun, X.; Curth, U.; Drosten, C.; Sauerhering, L.; Becker, S.; Rox, K.; Hilgenfeld, R. Crystal structure of SARS-CoV-2 main protease provides a basis for design of improved α-ketoamide inhibitors. *Science* **2020**, *368*, 409−412.
(27) Fu, L.; Ye, F.; Feng, Y.; Yu, F.; Wang, Q.; Wu, Y.; Zhao, C.; Sun, H.; Huang, B.; Niu, P.; Song, H.; Shi, Y.; et al. Both Boceprevir and GC376 efficaciously inhibit SARS-CoV-2 by targeting its main protease. *Nat. Commun.* **2020**, *11*, 4417.
(28) Jin, Z.; Zhao, Y.; Sun, Y.; Zhang, B.; Wang, H.; Wu, Y.; Zhu, Y.; Zhu, C.; Hu, T.; Du, X.; Duan, Y.; Yu, J.; Yang, X.; et al. Structural basis for the inhibition of SARS-CoV-2 main protease by antineoplastic drug carmofur. *Nat. Struct. Mol. Biol.* **2020**, *27*, 529−532.
(29) Aanouz, I.; Belhassan, A.; El-Khatabi, K.; Lakhlifi, T.; El-Ldrissi, M.; Bouachrine, M. Moroccan Medicinal plants as inhibitors against SARS-CoV-2 main protease: Computational investigations. *J. Biomol. Struct. Dyn.* **2021**, *39*, 2971−2979.
(30) Cao, W.; Cho, C.-C. D.; Geng, Z. Z.; Shaabani, N.; Ma, X. R.; Vatansever, E. C.; Alugubelli, Y. R.; Ma, Y.; Chaki, S. P.; Ellenburg, W. H.; Yang, K. S.; Qiao, Y.; Allen, R.; Neuman, B. W.; et al. Evaluation of SARS-CoV-2 main protease inhibitors using a novel cell-based assay. *ACS Cent. Sci.* **2022**, *8*, 192−204.
(31) Luttens, A.; Gullberg, H.; Abdurakhmanov, E.; Vo, D. D.; Akaberi, D.; Talibov, V. O.; Nekhotiaeva, N.; Vangeel, L.; De Jonghe, S.; Jochmans, D.; Krambrich, J.; Tas, A.; Lundgren, B.; et al. Ultralarge virtual screening identifies SARS-CoV-2 main protease inhibitors with broad-spectrum activity against coronaviruses. *J. Am. Chem. Soc.* **2022**, *144*, 2905−2920.
(32) Andrzejczyk, J.; Jovic, K.; Brown, L. M.; Pascetta, V. G.; Varga, K.; Vashisth, H. Molecular interactions and inhibition of the SARS-CoV-2 main protease by a thiadiazolidinone derivative. *Proteins* **2022**, *90*, 1896−1907.
(33) Scheuplein, N. J.; Bzdyl, N. M.; Kibble, E. A.; Lohr, T.; Holzgrabe, U.; Sarkar-Tyson, M. Targeting protein folding: a novel approach for the treatment of pathogenic bacteria. *J. Med. Chem.* **2020**, *63*, 13355−13388.
(34) Sun, Z.; Wang, L.; Li, X.; Fan, C.; Xu, J.; Shi, Z.; Qiao, H.; Lan, Z.; Zhang, X.; Li, L.; Zhou, X.; Geng, Y. An extended conformation of SARS-CoV-2 main protease reveals allosteric targets. *Proc. Natl. Acad. Sci. U.S.A.* **2022**, *119*, No. e2120913119.
(35) Zwanzig, R. W. High-temperature equation of state by a perturbation method. I. Nonpolar Gases. *J. Chem. Phys.* **1954**, *22*, 1420−1426.
(36) Kumar, A.; Mukherjee, D.; Satpati, P. Mutations in parkinson's disease associated protein DJ-1 alter the energetics of DJ-1 dimerization. *J. Chem. Inf. Model.* **2019**, *59*, 1497−1507.
(37) Kumar, A.; Vashisth, H. Conformational dynamics and energetics of viral RNA recognition by lab-evolved proteins. *Phys. Chem. Chem. Phys.* **2021**, *23*, 24773−24779.
(38) Kumar, A.; Vashisth, H. Role of mutations in differential recognition of viral RNA molecules by peptides. *J. Chem. Inf. Model.* **2022**, *62*, 3381−3390.
(39) Pal, S.; Kumar, A.; Vashisth, H. Role of dynamics and mutations in interactions of a zinc finger antiviral protein with CG-rich viral RNA. *J. Chem. Inf. Model.* **2023**, *63*, 1002−1011.
(40) Šali, A.; Blundell, T. L. Comparative protein modelling by satisfaction of spatial restraints. *J. Mol. Biol.* **1993**, *234*, 779−815.
(41) Humphrey, W.; Dalke, A.; Schulten, K. VMD: Visual Molecular Dynamics. *J. Mol. Graphics* **1996**, *14*, 33−38.
(42) Li, H.; Robertson, A. D.; Jensen, J. H. Very fast empirical prediction and rationalization of protein pKa values. *Proteins* **2005**, *61*, 704−721.
(43) Huang, J.; MacKerell, A. D. CHARMM36 all-atom additive protein force field: Validation based on comparison to NMR data. *J. Comput. Chem.* **2013**, *34*, 2135−2145.
(44) Darden, T.; York, D.; Pedersen, L. Particle Mesh Ewald: An Nlog(N) method for Ewald sums in large systems. *J. Chem. Phys.* **1993**, *98*, 10089−10092.
(45) Phillips, J. C.; Hardy, D. J.; Maia, J. D.; Stone, J. E.; Ribeiro, J. V.; Bernardi, R. C.; Buch, R.; Fiorin, G.; Hénin, J.; Jiang, W.; McGreevy, R.; Melo, M. C. R.; Radak, B. K.; et al. Scalable molecular dynamics on CPU and GPU architectures with NAMD. *J. Chem. Phys.* **2020**, *153*, 044130.
(46) Figueirido, F.; Del Buono, G. S.; Levy, R. M. On finite-size effects in computer simulations using the Ewald potential. *J. Chem. Phys.* **1995**, *103*, 6133−6142.
(47) Bogusz, S.; Cheatham, T. E.; Brooks, B. R. Removal of pressure and free energy artifacts in charged periodic systems via net charge corrections to the Ewald potential. *J. Chem. Phys.* **1998**, *108*, 7070−7084.
(48) Roe, D. R.; Cheatham, T. E. PTRAJ and CPPTRAJ: Software for processing and analysis of molecular dynamics trajectory data. *J. Chem. Theory Comput.* **2013**, *9*, 3084−3095.
(49) Schrödinger, L. *The PyMOL Molecular Graphics System*. version 1.8, 2015.
(50) Liu, P.; Dehez, F.; Cai, W.; Chipot, C. A toolkit for the analysis of free-energy perturbation calculations. *J. Chem. Theory Comput.* **2012**, *8*, 2606−2616.
(51) Kumar, A.; Vashisth, H. Mechanism of ligand discrimination by the NMT1 riboswitch. *J. Chem. Inf. Model.* **2023**, *63*, 4864−4874.

https://doi.org/10.1021/acs.jcim.3c01933
J. Chem. Inf. Model. 2024, 64, 2068−2076

(52) Matthews, J. M.; Fersht, A. R. Exploring the energy surface of protein folding by structure-reactivity relationships and engineered proteins: observation of Hammond behavior for the gross structure of the transition state and anti-Hammond behavior for structural elements for unfolding/folding of barnase. *Biochemistry* **1995**, *34*, 6805−6814.
(53) Fersht, A. R.; Sato, S. Φ-value analysis and the nature of protein-folding transition states. *Proc. Natl. Acad. Sci. U.S.A.* **2004**, *101*, 7976−7981.
(54) Johnson, Q. R.; Lindsay, R. J.; Nellas, R. B.; Fernandez, E. J.; Shen, T. Mapping allostery through computational glycine scanning and correlation analysis of residue−residue contacts. *Biochemistry* **2015**, *54*, 1534−1541.
(55) Morrison, K. L.; Weiss, G. A. Combinatorial alanine-scanning. *Curr. Opin. Chem. Biol.* **2001**, *5*, 302−307.
(56) DeLano, W. L. Unraveling hot spots in binding interfaces: progress and challenges. *Curr. Opin. Struct. Biol.* **2002**, *12*, 14−20.
(57) Moreira, I. S.; Fernandes, P. A.; Ramos, M. J. Hot spots—A review of the protein−protein interface determinant amino-acid residues. *Proteins* **2007**, *68*, 803−812.
(58) Edelheit, O.; Hanukoglu, I.; Dascal, N.; Hanukoglu, A. Identification of the roles of conserved charged residues in the extracellular domain of an epithelial sodium channel (ENaC) subunit by alanine mutagenesis. *Am. J. Physiol.: Renal Physiol.* **2011**, *300*, F887−F897.
(59) Hummer, G.; Pratt, L. R.; Garcia, A. E. Free energy of ionic hydration. *J. Phys. Chem.* **1996**, *100*, 1206−1215.
(60) Rocklin, G. J.; Mobley, D. L.; Dill, K. A.; Hünenberger, P. H. Calculating the binding free energies of charged species based on explicit-solvent simulations employing lattice-sum methods: An accurate correction scheme for electrostatic finite-size effects. *J. Chem. Phys.* **2013**, *139*, 184103.
(61) Phillips, J. C.; Braun, R.; Wang, W.; Gumbart, J.; Tajkhorshid, E.; Villa, E.; Chipot, C.; Skeel, R. D.; Kale, L.; Schulten, K. Scalable molecular dynamics with NAMD. *J. Comput. Chem.* **2005**, *26*, 1781−1802.

https://doi.org/10.1021/acs.jcim.3c01933
J. Chem. Inf. Model. 2024, 64, 2068−2076